

Lagrange–Chebyshev Interpolation for image resizing

Donatella Occorsio^{a,1}, Giuliana Ramella^b, Woula Themistoclakis^{b,*}

^a*Department of Mathematics and Computer Science, University of Basilicata, Viale dell’Ateneo
Lucano 10, 85100 Potenza, Italy*

^b*C.N.R. National Research Council of Italy, Institute for Applied Computing “Mauro Picone”, Via
P. Castellino, 111, 80131 Naples, Italy*

Abstract

Image resizing is a basic tool in image processing and in literature we have many methods, based on different approaches, which are often specialized in only upscaling or downscaling. In this paper, independently of the (reduced or enhanced) size we aim to get, we approach the problem at a continuous scale where the underlying continuous image is globally approximated by the tensor product Lagrange polynomial interpolating at a suitable grid of first kind Chebyshev zeros. This is a well-known approximation tool that is widely used in many applicative fields, due to the optimal behavior of the related Lebesgue constants. Here we show how Lagrange–Chebyshev interpolation can be fruitfully applied also for resizing an arbitrary digital image in both downscaling and upscaling. The performance of the proposed method has been tested in terms of the standard SSIM and PSNR metrics. The results indicate that, in upscaling, it is almost comparable with the classical Bicubic resizing method with slightly better metrics, but in downscaling a much higher performance has been observed in comparison with Bicubic and other recent methods too. Moreover, in downscaling cases with an odd scale factor, we give an estimate of the mean squared error produced by our method and prove it is theoretically null (hence PSNR equals to infinite and SSIM equals to one) in absence of noise or initial artifacts on the input image.

Keywords: Image resizing, Image downscaling, Image upscaling, Lagrange interpolation, Chebyshev nodes

2000 MSC: 94A08, 68U10, 41A05, 62H35

1. Introduction

In this paper, we deal with the problem of image resizing. This has been widely investigated over the past decades and is still an active research area characterized by many applications in different domains, including image transmission, satellite image

*The research has been accomplished within Research ITalian network on Approximation (RITA) and Approximation Theory research group of Unione Matematica Italiana (TA–UMI). It has been partially supported by GNCS–INdAM and University of Basilicata (local funds).

*Corresponding author

Email addresses: donatella.occorsio@unibas.it (Donatella Occorsio),
giuliana.ramella@cnr.it (Giuliana Ramella), woula.themistoclakis@cnr.it (Woula Themistoclakis)

analysis, gaming, remote sensing, etc. (see e.g. [8, 22, 25, 28, 50, 51]) In literature, downscaling and upscaling are often considered separate problems (see e.g. [7, 30, 50]), and most of the existing methods are specialized in only one direction, sometimes for a limited range of scaling factors (see e.g. [13, 46]). The method we are going to introduce works in both down and up scaling directions and for "large" scaling factors as well. It falls into the class of the interpolation methods and it is based on a non-standard modeling of the image resizing problem.

In order to introduce the adopted model we premise that, from the mathematical viewpoint, a continuous image \mathcal{I} is a function $f(x, y)$ of the spatial coordinates which, without losing the generality, we can assume belonging to the open square $A =]-1, 1[^2$. Hence, its digital version I of $n \times m$ pixels is supposed to be made of the values that f takes on a discrete grid of nodes $X_{n \times m} \subset A$. Regarding such grid, it is generally supposed that $X_{n \times m} = X_n \times X_m$ where we set

$$X_\mu := \{x_k^\mu : k = 1, \dots, \mu\} \subset]-1, 1[, \quad \forall \mu \in \mathbb{N}. \quad (1)$$

A typical and natural choice of the (univariate) system of nodes X_μ is to divide $[-1, 1]$ in $(\mu + 1)$ equal parts and to take the μ internal equidistant nodes, i.e.

$$X_\mu^{equ} = \left\{ -1 + \frac{2k}{\mu + 1} : k = 1, \dots, \mu \right\}. \quad (2)$$

However, it is well known that equally spaced nodes are not the best choice for Lagrange interpolation since they lead to exponentially growing Lebesgue constants, whereas optimal Lebesgue constants (growing at the minimal projection rate) are provided by the Chebyshev nodes of the first kind

$$x_k^\mu = \cos \left[\frac{(2k - 1)\pi}{2\mu} \right], \quad k = 1, \dots, \mu, \quad \forall \mu \in \mathbb{N}, \quad (3)$$

(see e.g. [27, 45] for a short excursion on the topic).

Discrete polynomial approximation based on Chebyshev zeros is a pillar in approximation theory and practices. It has been widely studied and applied in several fields and also recently, Chebyshev-like grids such as Xu points and Padua points have been introduced to get optimal interpolation processes on the square (see e.g. [48, 49, 9, 11, 33]). Nevertheless, to our knowledge, its usage in image processing has been mainly limited to particular cases, such as Magnetic Particle Imaging that is strictly related to Lissajous curves generating the Padua points (see e.g. [21, 18, 14]).

Indeed, at a first look, Chebyshev zeros may seem unsuitable for sampling an arbitrary image since they are not equidistant on the segment $] - 1, 1[$ of each spatial coordinate, but they are *arc sine* distributed, becoming denser at the endpoints ± 1 (see Figure 1). Nevertheless, in our model, we transfer the sampling question from the segment $] - 1, 1[$ to the semicircle of radius 1 centered at the axes origin. Thus, using the standard setting $t = \arccos x$, instead of the usual equidistant nodes on the segment, our method takes the following equidistant nodes on the semicircle

$$t_k^\mu := \frac{(2k - 1)\pi}{2\mu}, \quad k = 1, \dots, \mu, \quad \mu \in \mathbb{N}, \quad (4)$$

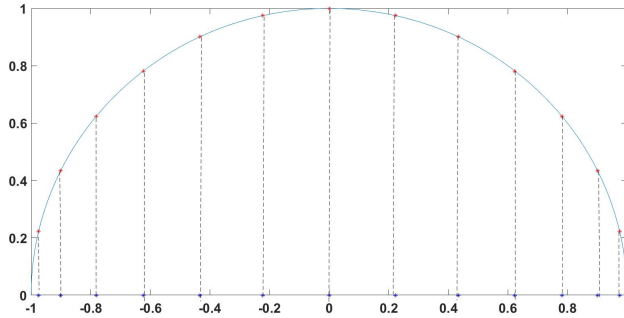


Figure 1: The first kind Chebyshev zeros of order $\mu = 15$ (black stars) and their arccosine (red stars)

These nodes define the Chebyshev zeros $x_k^\mu = \cos t_k^\mu$ in (3) and the grid

$$X_{n \times m} = \{(x_i^n, x_j^m) : i = 1 : n, j = 1 : m\}, \quad n, m \in \mathbb{N} \quad (5)$$

which we actually choose to sample arbitrary (continuous) images \mathcal{I} and to obtain digital images of $n \times m$ pixels, for arbitrary $n, m \in \mathbb{N}$.

According to this model, let $I = f(X_{n \times m})$ be the digital image of $n \times m$ pixels, i.e.

$$I_{i,j} := f(x_i^n, x_j^m), \quad i = 1 : n, j = 1 : m, \quad (6)$$

and let I^{in} be its more or less corrupted version really available as input data, say

$$I_{i,j}^{in} := \tilde{f}(x_i^n, x_j^m), \quad i = 1 : n, j = 1 : m, \quad (7)$$

where \tilde{f} denotes a corrupted version of the continuous image. Starting from the data I^{in} , the resizing problem aims to find a good approximation of the resampled image I^{res} consisting of the samples of f at the different (more or less dense) grid $X_{N \times M}$, i.e.

$$I_{k,h}^{res} := f(x_k^N, x_h^M), \quad k = 1 : N, h = 1 : M. \quad (8)$$

Hence, under our modeling, the resizing problem raises the following approximation question: starting from the approximate values of f at the Chebyshev grid $X_{n \times m}$, how to approximate f at another (coarser in downscaling or finer in upscaling) Chebyshev grid $X_{N \times M}$? The solution we propose relies on the global approximation of a function by its bivariate Lagrange polynomial interpolating at the Chebyshev grid $X_{n \times m}$.

This well-known interpolation polynomial can be easily deduced via tensor product from the univariate case (see for instance [31, 32, 34, 35]) and fast algorithms can be implemented for its computation (see e.g. [33]). Moreover, we recall that wavelets techniques can be applied to such kind of interpolation [20, 15, 16].

Hence, in order to get the resampled image, instead of f , we propose to sample a suitable Lagrange interpolation polynomial at the new grid. More precisely, we use the pixels of the input image I^{in} to build the Lagrange-Chebyshev polynomial $L_{n,m} \tilde{f}$ interpolating \tilde{f} at $X_{n \times m}$ and we get the output image of the desired $N \times M$ size (here denoted by I^{out}) by sampling $L_{n,m} \tilde{f}$ at the mesh $X_{N \times M}$.

To test the performance of such Lagrange-Chebyshev Interpolation (LCI) method we have considered the usual SSIM (Structured Similarity Index Measurement) and PSNR

(Peak Signal to Noise Ratio) metrics as computed by MatLab, and we have carried out the experimentation on several kinds of images collected in 5 datasets, having different characteristics on the size and the quality of the images, the variety of subjects, etc.

For an initial comparison, we focused on interpolation methods working as well in both down and up scaling directions. In general, these methods find a resized image by local or global interpolation of the continuous image f , using in some way the initial $n \times m$ pixels, namely the more or less corrupted values of f at the grid of nodes $X_{n \times m}$. Typically, for such grid it is assumed the equidistant nodes model (2) and most of the interpolation methods act locally on each pixel of the input image. This is the case of the classical bicubic interpolation method BIC [19] implemented by the Matlab built-in function `imresize` which we have used either in upscaling and downscaling to get a first comparison.

By the extensive experimentation we carried out, we assess that the performance of the LCI method is superior in downscaling (d-LCI method), while in upscaling (u-LCI method) there are only slight differences and the two methods seem almost comparable.

Thus it seemed relevant to us to further investigate only the downscaling case by testing d-LCI method in comparison with two other recent downscaling methods, here denoted by DPID [47] and L_0 [23], both of them not belonging to the family of interpolation methods for downscaling. The effective better performance in downscaling has been confirmed also in these cases, with an increasing gap as the downscaling factor increases. Moreover, by running the public available Matlab code, we have observed that DPID and L_0 methods work only for integer scale factors n/N and m/M and they are not always implementable for images with large sizes due to too long running times or too much memory. On the contrary, LCI method keeps the runtimes contained and offers high flexibility since it works in both downscaling and upscaling with non integer scale factors too, being possible to specify the desired final size or the scale factor as input parameters. We remark that similar nice features are shared by the Matlab function `imresize`, but with lower performances in downscaling. Moreover, in downscaling, for all odd scale factors, we state a theoretical estimate of the Mean Squared Error (MSE) obtained by our d-LCI method arriving to prove that it is null if $I^{in} = I$. Such a theoretical result has been confirmed by our experimentation that also shows it does not hold for `imresize` applied to the same input images.

The paper is organized as follows. For a simpler exposition of the idea behind the LCI method, we first introduce the method for a monochrome image in Section 2 and then, in Section 3, we expose it for RGB color images. Both monochrome and color cases are considered in Section 4 where some advantages of our approach are discussed. Finally, Section 5 consists of all the numerical experiments.

2. Re-sampling gray-level images

In the case of a monochrome image, \mathcal{I} is represented at a continuous scale by a scalar function $f(x, y)$ whose values are the grey levels at the spatial coordinates $(x, y) \in A$. Moreover, at a discrete scale, digital images of $n \times m$ pixels are matrices $I \in \mathbb{R}^{n \times m}$ whose elements are the samples of f at the discrete nodes set $X_{n \times m}$ defined in our model by (5) and (3). Then, according to the notation introduced in the previous section, the resizing problem of \mathcal{I} (in upscaling or in downscaling, respectively) consists in finding

a good approximation of the matrix $I^{res} \in \mathbb{R}^{N \times M}$ given by (8) starting from the matrix (having a reduced or enlarged size, respectively) $I^{in} \in \mathbb{R}^{n \times m}$ defined as in (7) being \tilde{f} a more or less corrupted version of f .

We approach such an approximation problem by using the following bivariate (tensor product) Lagrange–Chebyshev polynomial based on the available data I^{in}

$$L_{n,m}\tilde{f}(x, y) := \sum_{i=1}^n \sum_{j=1}^m \tilde{f}(x_i^n, x_j^m) \ell_i^n(x) \ell_j^m(y), \quad (x, y) \in A, \quad (9)$$

where, for all $\mu \in \mathbb{N}$, ℓ_k^μ denotes the k -th fundamental Lagrange polynomial related to the nodes system X_μ , namely

$$\ell_k^\mu(\xi) := \prod_{\substack{s=1 \\ s \neq k}}^{\mu} \frac{\xi - x_s^\mu}{x_k^\mu - x_s^\mu}, \quad \xi \in [-1, 1], \quad , \quad k = 1 : \mu. \quad (10)$$

It is well-known that the Lagrange–Chebyshev polynomial in (9) interpolates \tilde{f} at the grid $X_{n \times m}$, i.e.

$$L_{n,m}\tilde{f}(x_i^n, x_j^m) = \tilde{f}(x_i^n, x_j^m) = I_{i,j}^{in}, \quad i = 1 : n, \quad j = 1 : m. \quad (11)$$

The samples of such polynomial at the re-scaled grid $X_{N \times M}$ constitute the approximate resized image provided by the LCI method. Hence, the LCI method computes the matrix $I^{out} \in \mathbb{R}^{N \times M}$ whose entries are the following

$$I_{k,h}^{out} := L_{n,m}\tilde{f}(x_k^N, x_h^M), \quad k = 1 : N, \quad h = 1 : M. \quad (12)$$

Introducing the Vandermonde-like matrices

$$V_1 := [\ell_i^n(x_k^N)]_{i,k} \in \mathbb{R}^{n \times N}, \quad V_2 := [\ell_j^m(x_h^M)]_{j,h} \in \mathbb{R}^{m \times M}, \quad (13)$$

by (9) and (12), the output matrix I^{out} can be computed from the input matrix I^{in} according to the following matrices identity

$$I^{out} = V_1^T I^{in} V_2, \quad (14)$$

Note that in case we have to resize a lot of images for the same fixed sizes, formula (14) also allows working in parallel with pre-computed matrices V_i .

Moreover, it is well known that the fast computation of the matrices V_i can be achieved by using, instead of (10), the following more convenient form of the fundamental Lagrange polynomial

$$\ell_k^\mu(\cos t) = \frac{2}{\mu} \sum_{r=0}^{\mu-1}{}' \cos \left[\frac{(2k-1)r\pi}{2\mu} \right] \cos [rt], \quad k = 1 : \mu, \quad t \in [0, \pi], \quad (15)$$

where, as usual, the prime on the summation symbol means that the first addendum is halved. Hence, by (15) we get that the matrices V_1 and V_2 can be computed by using

fast cosine transform algorithms (see e.g. [37]) being

$$(V_1)_{i,k} = \ell_i^n(x_k^N) = \frac{2}{n} \sum_{r=0}^{n-1} \cos \left[\frac{(2i-1)r\pi}{2n} \right] \cos \left[\frac{(2k-1)r\pi}{2N} \right], \quad (16)$$

$$i = 1 : n, \quad k = 1 : N,$$

$$(V_2)_{j,h} = \ell_j^m(x_h^M) = \frac{2}{m} \sum_{s=0}^{m-1} \cos \left[\frac{(2j-1)s\pi}{2m} \right] \cos \left[\frac{(2h-1)s\pi}{2M} \right], \quad (17)$$

$$j = 1 : m, \quad h = 1 : M.$$

3. Re-sampling RGB color images

Now we are going to introduce the method for a general color image \mathcal{I} . In this case, behind \mathcal{I} there is a vector function $\mathbf{f} : A \rightarrow \mathbb{R}^3$ whose components $\mathbf{f} = (f_R, f_G, f_B)$ represent \mathcal{I} in the RGB color space. According to our model, the input image \mathbf{I}^{in} and the target resized image \mathbf{I}^{res} are represented in the RGB space as the follows

$$\mathbf{I}^{in} \in \mathbb{R}^{n \times m \times 3}, \quad \mathbf{I}^{in} \equiv (I_R^{in}, I_G^{in}, I_B^{in})$$

$$\mathbf{I}^{res} \in \mathbb{R}^{N \times M \times 3}, \quad \mathbf{I}^{res} \equiv (I_R^{res}, I_G^{res}, I_B^{res}),$$

where we assume that

$$\begin{aligned} (I_R^{in})_{i,j} &= \tilde{f}_R(x_i^n, x_j^m), & (I_R^{res})_{k,h} &= f_R(x_k^N, x_h^M), \\ (I_G^{in})_{i,j} &= \tilde{f}_G(x_i^n, x_j^m), & (I_G^{res})_{k,h} &= f_G(x_k^N, x_h^M), \\ (I_B^{in})_{i,j} &= \tilde{f}_B(x_i^n, x_j^m), & (I_B^{res})_{k,h} &= f_B(x_k^N, x_h^M). \end{aligned} \quad (18)$$

holds for all $[i, j] = [1 : n, 1 : m]$ and $[k, h] = [1 : N, 1 : M]$.

Thus, similarly to the monochrome case and with obvious meaning of the notation, we start from

$$\mathbf{I}_{i,j}^{in} = \tilde{\mathbf{f}}(x_i^n, x_j^m) \quad i = 1 : n, \quad j = 1 : m, \quad (19)$$

and approximate \mathbf{I}^{res} by

$$\mathbf{I}_{k,h}^{out} = L_{n,m} \tilde{\mathbf{f}}(x_k^N, x_h^M) \quad k = 1 : N, \quad h = 1 : M \quad (20)$$

i.e., for $k = 1 : N$ and $h = 1 : M$, we define

$$\mathbf{I}_{k,h}^{out} = \left(L_{n,m} \tilde{f}_R(x_k^N, x_h^M), L_{n,m} \tilde{f}_G(x_k^N, x_h^M), L_{n,m} \tilde{f}_B(x_k^N, x_h^M) \right). \quad (21)$$

Hence, by applying the same argument of the monochrome case, we get that the RGB components of the output image $\mathbf{I}^{out} \equiv (I_R^{out}, I_G^{out}, I_B^{out})$ are given by

$$\mathbf{I}^{out} = (V_1^T I_R^{in} V_2, V_1^T I_G^{in} V_2, V_1^T I_B^{in} V_2),$$

with V_1, V_2 defined in (16)–(17).

4. Model analysis

For a general analysis of the error we get in approximating the target resized image $I^{res} = [\mathbf{f}(x_i^n, x_j^m)]_{i,j}$ with the output image $I^{out} = [\mathbf{L}_{n,m}\tilde{\mathbf{f}}(x_h^N, x_k^M)]_{h,k}$ produced by LCI method, we refer the reader to the wide existing literature on the Lagrange interpolation error estimates (see e.g. [27] and the references therein). In this paper, we are interested to measure the performance of LCI method through some standard metrics usually used in Image Processing (see e.g. [38] and the references therein). In particular, we focus on the Mean Squared Error (MSE) defined as follows

$$\text{MSE}(\mathbf{I}^{res}, \mathbf{I}^{out}) = \begin{cases} \frac{1}{MN} \|\mathbf{I}^{res} - \mathbf{I}^{out}\|_F^2, & \text{gray-level images,} \\ \frac{1}{3NM} \{ \|\mathbf{I}_R^{res} - \mathbf{I}_R^{out}\|_F^2 + \|\mathbf{I}_G^{res} - \mathbf{I}_G^{out}\|_F^2 + \|\mathbf{I}_B^{res} - \mathbf{I}_B^{out}\|_F^2 \}, & \text{RGB color images,} \end{cases}$$

being $\|\cdot\|_F$ the Frobenius norm

$$\|A\|_F := \left(\sum_{k=1}^N \sum_{h=1}^M A_{k,h}^2 \right)^{\frac{1}{2}}, \quad A = (A_{k,h}) \in \mathbb{R}^{N \times M}.$$

Moreover, we consider the Peak Signal to Noise Ratio (PSNR) defined by the previous MSE as follows

$$\text{PSNR}(\mathbf{I}^{res}, \mathbf{I}^{out}) = 20 \log_{10} \left(\frac{\max_f}{\sqrt{\text{MSE}(\mathbf{I}^{res}, \mathbf{I}^{out})}} \right), \quad (22)$$

with $\max_f = 255$, since we use the representation by 8 bits per sample.

Finally, in our experiments we evaluate the Structured Similarity Index Measurement (SSIM). For grey-level images it is defined as

$$\text{SSIM}(\mathbf{I}^{res}, \mathbf{I}^{out}) = \frac{[2\mu(\mathbf{I}^{res})\mu(\mathbf{I}^{out}) + c_1][2\text{cov}(\mathbf{I}^{res}, \mathbf{I}^{out}) + c_2]}{[\mu^2(\mathbf{I}^{res}) + \mu^2(\mathbf{I}^{out}) + c_1][\sigma^2(\mathbf{I}^{res}) + \sigma^2(\mathbf{I}^{out}) + c_2]}, \quad (23)$$

where $\mu(A)$, $\sigma(A)$ and $\text{cov}(A, B)$ indicate the average, variance and covariance, respectively, of the matrices A, B , and c_1, c_2 are constants usually fixed as $c_1 = (0.01 \times L)$, $c_2 = (0.03 \times L)$ with the dynamic range of the pixel values $L = 255$ for 8-bit images.

In the case of RGB color images, making the conversion to the color space YCbCr, the SSIM is computed by the above definition applied to the intensity Y (luma) channel.

Based on the previous metrics, the results of wide experimentation will be reported in the next section. In the sequel, we are going to underly two particular features of LCI method.

A first aspect is related to the model choice which, for odd downscaling factors $s := n/N = m/M > 1$, leads to state the following

Proposition 4.1. *Under the previously introduced notation, if there exists $\ell \in \mathbb{N}$ s.t. $n = (2\ell - 1)N$ and $m = (2\ell - 1)M$ hold, then we have*

$$\text{MSE}(\mathbf{I}^{res}, \mathbf{I}^{out}) \leq s^2 \text{MSE}(\mathbf{I}, \mathbf{I}^{in}), \quad s := (2\ell - 1). \quad (24)$$

Moreover, if $I = I^{in}$ then we get the best results

$$\text{MSE}(I^{\text{res}}, I^{\text{out}}) = 0, \quad \text{and} \quad \text{SSIM}(I^{\text{res}}, I^{\text{out}}) = 1. \quad (25)$$

Proof. Let's give the proof in the case of a gray-level image since for RGB color images the statement will easily follow by considering the single RGB components.

As a keynote of the proof, we observe that for any $\ell \in \mathbb{N}$, we have

$$n = (2\ell - 1)N \quad \implies \quad X_N \subset X_n.$$

More precisely, setting $s := (2\ell - 1)$, it is easy to check that

$$n = sN \quad \implies \quad x_k^N = x_i^n \quad \text{with} \quad i = \frac{s(2k - 1) + 1}{2}, \quad k = 1 : N, \quad (26)$$

where we remark that for all $k = 1 : N$, the numerator $s(2k - 1) + 1$ is certainly even since s is odd.

Consequently, we deduce (24) from (26) as follows

$$\begin{aligned} \text{MSE}(I^{\text{res}}, I^{\text{out}}) &= \frac{1}{NM} \sum_{k=1}^N \sum_{h=1}^M \left[f(x_k^N, x_h^M) - L_{n,m} \tilde{f}(x_k^N, x_h^M) \right]^2 \\ &= \frac{1}{NM} \sum_{k=1}^N \sum_{h=1}^M \left[f\left(x_{\frac{s(2k-1)+1}{2}}^n, x_{\frac{s(2h-1)+1}{2}}^m\right) - \tilde{f}\left(x_{\frac{s(2k-1)+1}{2}}^n, x_{\frac{s(2h-1)+1}{2}}^m\right) \right]^2 \\ &\leq \frac{1}{NM} \sum_{i=1}^n \sum_{j=1}^m \left[f(x_i^n, x_j^m) - \tilde{f}(x_i^n, x_j^m) \right]^2 = s^2 \text{MSE}(I, I^{in}). \end{aligned}$$

Moreover, in the case that $I = I^{in}$, we have that $L_{n,m} f = L_{n,m} \tilde{f}$ and, due to the nesting property $X_{N \times M} \subset X_{n \times m}$, by (11), for any $h = 1 : N$ and $k = 1 : M$, we get

$$I_{h,k}^{\text{out}} = L_{n,m} \tilde{f}(x_h^N, x_k^M) = L_{n,m} f(x_h^N, x_k^M) = f(x_h^N, x_k^M) = I_{h,k}^{\text{res}}, \quad (27)$$

that implies the first equation in (25). Finally, (27) also yields

$$2\text{cov}(I^{\text{res}}, I^{\text{out}}) = \sigma(I^{\text{res}})^2 + \sigma(I^{\text{out}})^2,$$

$$2\mu(I^{\text{res}})\mu(I^{\text{out}}) = \mu(I^{\text{res}})^2 + \mu(I^{\text{out}})^2$$

which conclude the proof of (25). \diamond

We remark that the previous proposition is a direct consequence of our choice of the sampling model based on Chebyshev zeros (3), instead of the usual equally spaced nodes (2).

Such choice (and more generally the choice of "good" interpolation knots) allows to use global interpolation processes that are not possible in the case of equally spaced nodes. In fact, as second aspect, we aim to highlight the relevance of the choice of good interpolation knots by showing the effects we have in the performance of global Lagrange interpolation methods associated with the univariate nodes set X_μ^{equ} in (2). The disastrous effects of the exponential growth of Lebesgue constants are visible in

the next experiment concerning an image zooming $\times 2$ from the size $n \times n$ with $n = 256$ to the size $N \times N$ with $N = 512$. Figure 2 displays the images obtained starting from the same input image (Fig.2, left) and using the Lagrange interpolation polynomial based on equally spaced nodes $X_n^{equ} \times X_n^{equ}$ (Fig.2, right) and on the Chebyshev grid $X_{n \times n}$ (Fig.2, middle). The images we see are the samples of the previous Lagrange polynomials at the respective $(N \times N)$ -grid and we can check how the equally-spaced sampling model (2) yields wrong results outside of a small region of the output image.



Figure 2: The well-known image *Flowers* taken from USC-SIPI [1] (left) upsampled at the double scale by Lagrange interpolation at Chebyshev nodes (middle) and at equally spaced nodes (right)

5. Experimental results

In this section, we propose a selection of the extensive experimentation we carried on to test the benefits of our procedure in downscaling (d-LCI method) and in upscaling (u-LCI method), comparing our results with other resizing techniques.

5.1. Comparison methods

As already mentioned, we compare LCI with BIC provided by MatLab `imresize` with 'bicubic' option where we recall that a new pixel is determined from a weighted average of the 16 closest pixels using an interpolating cubic convolution function satisfying prescribed assumptions of smoothness on f to gain at least a cubic order of convergence [19]. The comparison BIC-LCI regards either down and up resizing cases, giving as input either the scale factor or the final size of the desired image. Note that we have also tested the other different options of `imresize` (namely 'linear' and 'nearest neighborhood') but for brevity, we do not report the results since they give no new insight.

Moreover, to further investigate the performance in downscaling case, we compare d-LCI with other two recent downscaling methods not belonging to the interpolation method class. These methods are briefly indicated as DPID method (described in [47] with the code available at [2]) and L_0 method (described in [23], with the code available at [3]). To be fair, we remark that we forced DPID and L_0 also in upscaling direction for several scaling factors (the choice of the desired size is not allowed by DPID and L_0) but the results were very poor w.r.t. BIC and LCI and they have been not reported here.

Finally, we point out that all the previous methods have run on the same PC with Intel Core i7 3770K CPU @350GHz configuration.

5.2. Datasets

Since the results of any method depend on the type of input image, we have conducted the experimentation on different kinds of 8–bits images collected in five publicly available datasets, whose characteristics (acronym, number of images, range of their sizes) are synthesized in Table 1.

Table 1: Datasets list

Dataset	n. of Images	Sizes
BSDS500	500	481×321 or 321×481
NASA	17	from 500×334 to 6394×3456
YAHOO	96	from 500×334 to 6394×3456
13US	13	from 241×400 to 400×310
URBAN100	100	from 1024×564 to 1024×1024

We point out that we have chosen the datasets in Table 1 since they are the same considered in [47, 23] for DPID and L_0 methods. In particular:

- BSDS500 dataset [26], available at [4], has been used for testing L_0 in [23]. It is sufficiently general and provides a large variety of images often employed for testing many other methods with different image analysis tasks such as image segmentation [29, 39, 40, 42]), color quantization [12, 41, 10, 43], etc.
- NASA Image Gallery [6] and YFCC100M (Yahoo Flickr Creative Commons 100 Million) [44] datasets (here briefly denoted by NASA and YAHOO, respectively) are used by DPID in [47].
- 13US [36] contains natural images, available at [5] and originally taken from the MSRA Salient Object Database [24]. It is another dataset used in [47].
- URBAN100 dataset [17], concerning urban scenes with images having one dimension equal to 1024, is commonly used to evaluate the performance of super-resolution models. It is used as test images for L_0 in [23].

All the previous datasets have been considered for either up and down scaling.

We remark that in all the performed experiments the input images are not available from the datasets. Hence, following a typical approach in image quantitative evaluation, we fix all the images from the datasets as target images (i.e. I^{res} in our notation) and we apply BIC to generate the input image (namely I^{in}) common to all methods. More precisely, to run $[\times s]$ upscaling methods ($[: s]$ downscaling methods, resp.) we generate the input image I^{in} by applying BIC to I^{res} in the opposite $[: s]$ ($[\times s]$, resp.) scaling direction.

Note that, according to such procedure, in testing $[\times s]$ upscaling methods we may find that I^{res} does not have both the dimensions N and M that are divisible for s . In this case, in order to generate I^{in} we use `imresize` with the size option, requiring $n = \lfloor \frac{N}{s} \rfloor$ and $m = \lfloor \frac{M}{s} \rfloor$. Moreover, once obtained I^{in} , both BIC and u-LCI run by specifying again the size $N \times M$ instead of the scaling factor.

5.3. Visual comparison

As first experiment, we focus on the visual comparison of some original images chosen in the previous datasets with the output images produced by the methods in Subsection 5.1. Such images are given in Figure 3 for upscaling and in Figure 4 for downscaling.

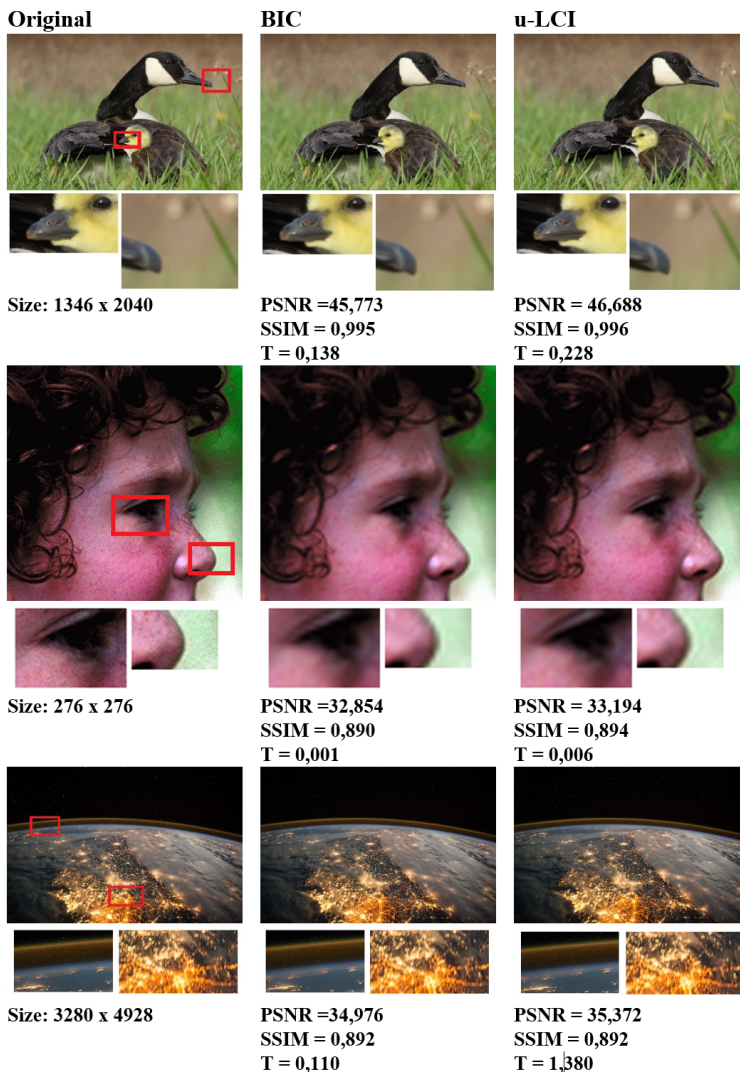


Figure 3: Examples of upscaling performance results at the scale factor 2 (top), at the scale factor 3 (middle), at the scale factor 4 (bottom).

In both the figures at the first column we show the target images and at the successive columns we display the resized images obtained as the output of the considered methods. Moreover, the first, second and third row of both the figures correspond to the scaling factors 2, 3 and 4, respectively. In all the cases the images have been reported with evidence of some magnified regions of interest (ROI).

From the qualitative point of view, by inspecting Figures 3 and 4, we can deduce that in terms of visual quality LCI has a good performance, also with respect to the chosen comparing methods. It preserves the visual structure of the object without losing image details, the local contrast, and the luminance of the input image, by generating resized images close to the target ones. Ringing and over smoothing artifacts are limited and

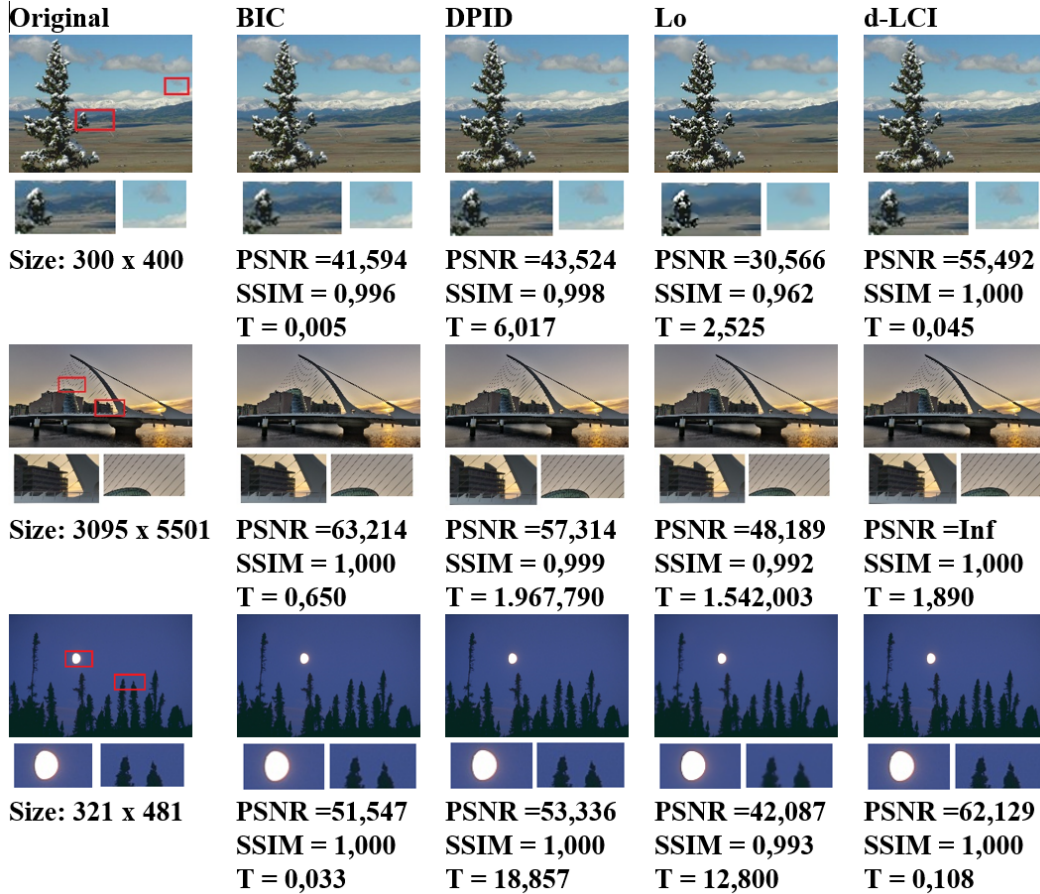


Figure 4: Examples of downscaling performance results at the scale factor 2 (top), at the scale factor 3 (middle), at the scale factor 4 (bottom).

the resized images seem fair, sufficiently not blurred, and with well-balanced colors.

5.4. Quantitative comparison: average results

For each dataset selected in Subsection 5.2, we computed the averages of the PSNR and SSIM values achieved by LCI and by the comparison methods described in Subsection 5.1, for the scaling factors 2, 3, 4. The results are displayed in Table 2 for upscaling and in Table 3 for downscaling, reporting in both the tables also the averages of the required CPU times.

As announced in the introduction, from Table 2 we see that the values attained by u-LCI are only slightly better than those achieved by BIC, and the execution time of u-LCI is a little bit greater than BIC. Of course, as the scale factor increases, both PSNR and SSIM decrease in all the upscaling methods. Moreover, the gaps between BIC and u-LCI in both the metrics are maintained also for large size images.

On the contrary, in downscaling, by inspecting Table 3 we observe that the performance provided by d-LCI is much better than those achieved by the other methods for both the metrics. In particular, when the downscaling factor is 3 the theoretical results claimed in Proposition 4.1 are confirmed. Moreover, looking at the even downscaling factors 2, 4 the improvement by d-LCI seems to increase as the scale factor increases

Table 2: Average results in upscaling.

	x2			x3			x4		
	PSNR	SSIM	T	PSNR	SSIM	T	PSNR	SSIM	T
BSDS500									
BIC	26,341	0,886	0,003	24,821	0,837	0,002	22,251	0,701	0,003
u-LCI	26,381	0,888	0,014	24,868	0,839	0,010	22,446	0,769	0,008
NASA									
BIC	34,806	0,958	0,091	31,205	0,924	0,074	29,808	0,907	0,071
u-LCI	35,412	0,960	1,357	31,542	0,924	0,839	30,183	0,908	0,634
YAHOO									
BIC	33,391	0,953	0,056	29,754	0,913	0,055	28,741	0,891	0,051
u-LCI	33,900	0,955	0,812	29,956	0,914	0,567	28,986	0,891	0,459
URBAN100									
BIC	25,433	0,882	0,009	21,306	0,755	0,008	21,703	0,741	0,008
u-LCI	25,896	0,886	0,064	21,325	0,754	0,051	21,919	0,793	0,059
13US									
BIC	24,116	0,861	0,002	20,754	0,734	0,002	20,545	0,710	0,002
u-LCI	24,486	0,868	0,012	20,780	0,738	0,010	20,656	0,713	0,009

Table 3: Average results in downscaling

	:2			:3			:4		
	PSNR	SSIM	T	PSNR	SSIM	T	PSNR	SSIM	T
BSDS500									
BIC	38,872	0,993	0,006	39,253	0,993	0,009	39,183	0,993	0,017
DPID	41,745	0,996	7,696	41,827	0,996	12,246	41,206	0,996	18,615
L ₀	29,317	0,961	3,647	32,873	0,971	8,020	34,174	0,971	14,295
d-LCI	53,732	1,000	0,057	Inf	1,000	0,091	55,889	1,000	0,137
NASA									
BIC	45,969	0,995	0,229	47,114	0,996	0,325	46,973	0,996	0,639
DPID	47,675	0,998	448,023	47,657	0,998	731,498	47,112	0,997	1.098,113
L ₀	34,754	0,972	208,574	37,285	0,979	617,386	oom	oom	oom
d-LCI	54,265	0,999	6,614	Inf	1,000	13,317	57,491	1,000	22,859
YAHOO									
BIC	44,757	0,996	0,155	45,858	0,997	0,219	45,682	0,996	0,422
DPID	46,743	0,998	291,685	46,948	0,998	479,638	46,421	0,998	714,908
L ₀	33,913	0,974	133,190	oom	oom	oom	oom	oom	oom
d-LCI	54,067	0,999	4,698	Inf	1,000	8,279	57,223	1,000	13,898
URBAN00									
BIC	35,661	0,989	0,027	36,010	0,990	0,041	35,940	0,989	0,068
DPID	39,178	0,996	37,592	39,178	0,996	60,834	38,702	0,995	93,996
L ₀	26,718	0,951	13,267	31,061	0,969	28,845	33,571	0,973	50,312
d-LCI	52,613	0,999	0,234	Inf	1,000	0,416	55,452	1,000	0,618
13US									
BIC	35,129	0,990	0,005	35,469	0,991	0,009	35,397	0,991	0,013
DPID	38,061	0,996	5,593	38,326	0,996	8,905	37,707	0,995	13,819
L ₀	25,521	0,949	2,572	30,231	0,972	5,706	32,929	0,979	9,939
d-LCI	52,813	1,000	0,042	Inf	1,000	0,073	55,374	1,000	0,108

while BIC seems to be affected by saturation, with an increasing gap between d-LCI and the remaining methods.

About the CPU time, except for BIC, d-LCI is faster than the other methods that, in case of very large images, need very long computational time (see the results for NASA and YAHOO datasets that include target images of size 6394×3456 , i.e. input images with size 25576×13824 in case of downscaling factor equals to 4) and in some cases, wherever we see oom (which means out of memory), the available code of L₀ does not arrive to produce any result.

5.5. Quantitative comparison: some pointwise results

Here we focus on each single image from the smaller datasets of Table 1, namely we consider 13US dataset in downscaling, with target images of small size displayed in

Figure 5, and NASA dataset in upscaling, with target images of large size displayed in Figure 6.



Figure 5: 13US dataset image: [U1 -U13] from left to right and from top to bottom .

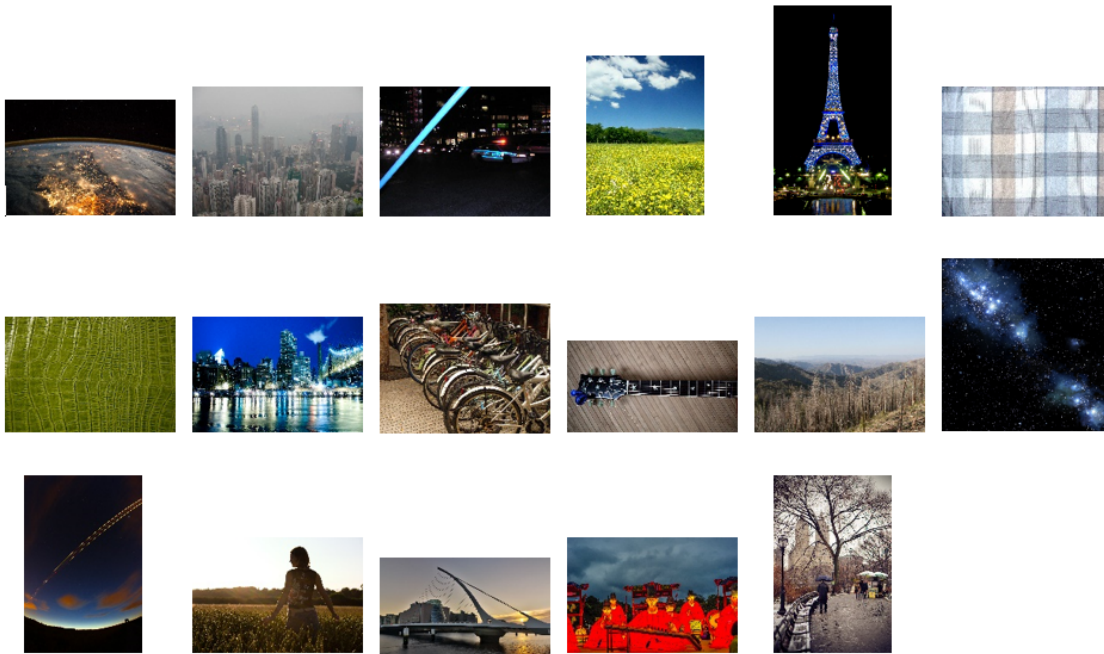


Figure 6: NASA dataset images: [N1, N2, N3, N5, N6, N7, N8, N9, N10, N11, N12, N13, N14, N15, N16, N17, N19] from left to right and from top to bottom .

The PSNR values achieved for every single image have been plotted in Figure 7 for NASA dataset with upscaling factor 2, 4, 8, 16, and in Figure 8 for 13US dataset with downscaling factor 6, 18, 30.

On the same datasets, more detailed results are given in Tables 4–6 reporting in the first columns the name and the size of all the images from 13US and NASA.

In particular, Table 4 contains the detailed upscaling results on the NASA dataset, for the scaling factors $s \in \{2, 4, 8, 16\}$ while Tables 5-6 concern the downscaling results

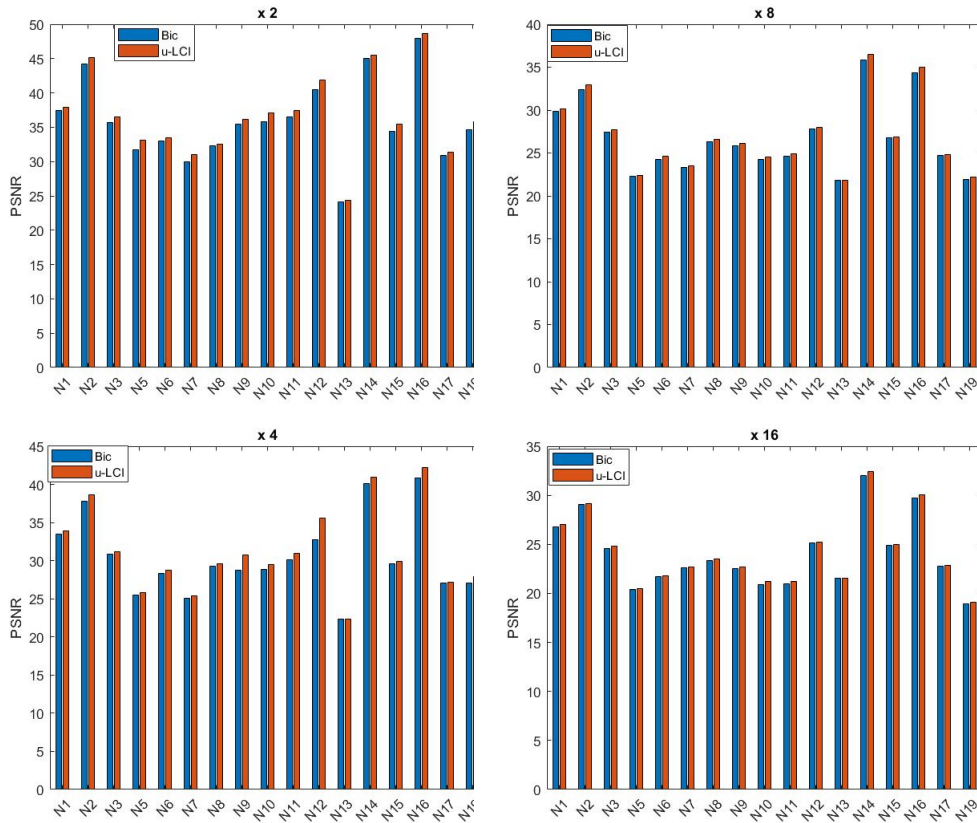


Figure 7: Pointwise PSNR for the NASA set for scale factors $s=2,4,8,16$

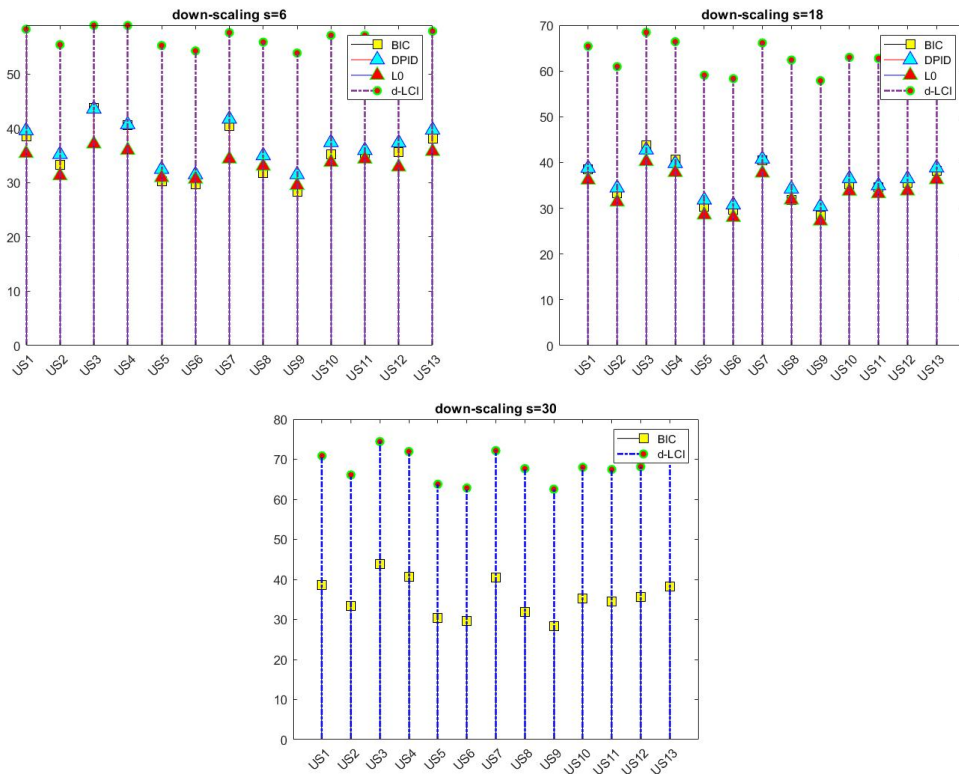


Figure 8: Pointwise PSNR values for the set 13US, with scale factors $s=6$ (top), $s=18$ (middle), $s=30$ (down)

Table 4: Pointwise results on NASA dataset in upscaling

	x2		x4		x8		x16	
	PSNR	SSIM	PSNR	SSIM	PSNR	SSIM	PSNR	SSIM
N1 4928×3280								
BIC	37,472	0,945	33,453	0,892	29,828	0,858	26,795	0,833
u-LCI	37,903	0,950	33,856	0,892	30,133	0,855	26,999	0,831
N2 3072×2304								
BIC	44,235	0,986	37,820	0,952	32,417	0,888	29,065	0,840
u-LCI	45,203	0,988	38,621	0,957	32,943	0,894	29,183	0,840
N3 2048×1536								
BIC	35,708	0,963	30,845	0,919	27,474	0,874	24,593	0,830
u-LCI	36,552	0,965	31,136	0,916	27,731	0,865	24,850	0,808
N5 2701×3665								
BIC	31,743	0,987	25,444	0,960	22,262	0,932	20,388	0,913
u-LCI	33,077	0,989	25,792	0,962	22,426	0,933	20,487	0,913
N6 1836×3264								
BIC	33,011	0,986	28,291	0,965	24,250	0,927	21,677	0,886
u-LCI	33,443	0,986	28,779	0,961	24,614	0,908	21,784	0,850
N7 1600×1200								
BIC	29,939	0,886	25,087	0,670	23,364	0,567	22,627	0,545
u-LCI	30,981	0,905	25,409	0,684	23,542	0,569	22,683	0,546
N8 3008×2000								
BIC	32,298	0,987	29,295	0,974	26,346	0,956	23,345	0,932
u-LCI	32,577	0,988	29,594	0,976	26,619	0,958	23,508	0,933
N9 5430×3520								
BIC	35,440	0,985	28,707	0,945	24,336	0,883	22,494	0,846
u-LCI	36,116	0,986	30,735	0,955	26,121	0,899	22,712	0,845
N10 3264×2448								
BIC	35,758	0,973	28,875	0,916	24,213	0,837	20,914	0,767
u-LCI	37,047	0,977	29,531	0,920	24,529	0,838	21,187	0,768
N11 4368×2326								
BIC	36,525	0,982	30,149	0,955	24,649	0,906	20,966	0,849
u-LCI	37,461	0,981	30,986	0,951	24,918	0,897	21,193	0,846
N12 3504×2336								
BIC	40,471	0,989	32,786	0,951	27,777	0,888	25,116	0,850
u-LCI	41,889	0,991	35,581	0,956	27,982	0,890	25,191	0,851
N13 1200×1600								
BIC	24,145	0,746	22,370	0,603	21,838	0,530	21,555	0,483
u-LCI	24,316	0,730	22,390	0,592	21,852	0,529	21,579	0,486
N14 3456×5184								
BIC	45,041	0,992	40,137	0,986	35,808	0,978	31,982	0,967
u-LCI	45,539	0,992	40,907	0,986	36,531	0,978	32,407	0,966
N15 3072×2048								
BIC	34,457	0,990	29,574	0,967	26,731	0,941	24,886	0,920
u-LCI	35,427	0,991	29,872	0,968	26,883	0,940	24,976	0,919
N16 5501×3095								
BIC	47,929	0,993	40,846	0,982	34,304	0,961	29,760	0,940
u-LCI	48,691	0,994	42,202	0,983	35,029	0,961	30,027	0,939
N17 2048×1363								
BIC	30,892	0,980	27,028	0,954	24,688	0,927	22,895	0,899
u-LCI	31,380	0,981	27,219	0,954	24,834	0,927	21,044	0,877
N19 3039×4559								
BIC	34,581	0,977	27,048	0,884	21,873	0,718	18,910	0,615
u-LCI	35,844	0,981	27,881	0,896	22,178	0,723	19,077	0,617

Table 5: Pointwise results on 13US dataset in downscaling

	:3		:6		:9		:18	
	PSNR	SSIM	PSNR	SSIM	PSNR	SSIM	PSNR	SSIM
US1 300×400								
BIC	38,625	0,996	38,573	0,996	38,583	0,996	38,584	0,996
DPID	40,846	0,997	39,580	0,997	39,160	0,996	38,764	0,996
L ₀	27,994	0,949	35,405	0,983	35,138	0,986	36,183	0,991
d-LCI	Inf	1,000	58,265	1,000	Inf	1,000	65,394	1,000
US2 400×300								
BIC	33,348	0,987	33,298	0,987	33,303	0,987	33,302	0,987
DPID	36,428	0,994	35,217	0,992	34,823	0,992	34,450	0,991
L ₀	29,184	0,963	31,289	0,967	30,647	0,968	31,394	0,977
d-LCI	Inf	1,000	55,418	1,000	Inf	1,000	60,956	1,000
US3 300×400								
BIC	43,820	0,999	43,754	0,999	43,774	0,999	43,786	0,999
DPID	44,853	0,999	43,589	0,999	43,162	0,999	42,751	0,999
L ₀	34,756	0,992	37,140	0,995	38,087	0,996	40,237	0,998
d-LCI	Inf	1,000	58,958	1,000	Inf	1,000	68,436	1,000
US4 300×400								
BIC	40,673	0,996	40,623	0,996	40,631	0,996	40,633	0,996
DPID	42,066	0,998	40,699	0,997	40,236	0,997	39,794	0,996
L ₀	32,944	0,973	35,973	0,981	36,453	0,986	37,836	0,992
d-LCI	Inf	1,000	58,958	1,000	Inf	1,000	66,386	1,000
US5 400×300								
BIC	30,357	0,979	30,307	0,979	30,311	0,979	30,311	0,979
DPID	33,492	0,991	32,471	0,989	32,133	0,988	31,813	0,987
L ₀	26,807	0,962	30,944	0,973	28,911	0,963	28,551	0,965
d-LCI	Inf	1,000	55,257	1,000	Inf	1,000	59,065	1,000
US6 300×400								
BIC	29,718	0,978	29,659	0,978	29,633	0,978	29,663	0,978
DPID	32,578	0,990	31,486	0,988	31,111	0,987	30,752	0,985
L ₀	25,322	0,959	30,666	0,966	28,724	0,958	28,022	0,962
d-LCI	Inf	1,000	54,273	1,000	Inf	1,000	58,321	1,000
US7 273×400								
BIC	40,559	0,995	40,513	0,995	40,521	0,995	40,522	0,995
DPID	43,135	0,997	41,717	0,996	41,232	0,996	40,771	0,996
L ₀	31,832	0,949	34,364	0,964	35,604	0,975	37,697	0,987
d-LCI	Inf	1,000	57,639	1,000	Inf	1,000	66,113	1,000
US8 322×400								
BIC	31,857	0,989	31,802	0,989	31,808	0,989	31,808	0,989
DPID	36,382	0,996	34,979	0,994	34,601	0,994	34,239	0,993
L ₀	29,562	0,974	33,051	0,977	32,378	0,980	31,828	0,985
d-LCI	Inf	1,000	55,880	1,000	Inf	1,000	62,394	1,000
US9 322×400								
BIC	28,407	0,984	28,350	0,984	28,536	0,984	28,354	0,984
DPID	32,542	0,994	31,504	0,993	34,601	0,992	30,393	0,992
L ₀	29,562	0,974	29,504	0,985	27,361	0,980	27,214	0,979
d-LCI	Inf	1,000	53,879	1,000	Inf	1,000	57,877	1,000
US10 400×307								
BIC	35,220	0,992	35,168	0,992	35,172	0,992	35,173	0,992
DPID	38,947	0,997	37,406	0,996	36,929	0,995	36,494	0,995
L ₀	31,031	0,984	33,760	0,986	33,227	0,985	33,744	0,988
d-LCI	Inf	1,000	57,131	1,000	Inf	1,000	62,986	1,000
US11 400×241								
BIC	34,599	0,995	34,528	0,995	34,536	0,995	34,535	0,995
DPID	37,345	0,998	35,950	0,997	35,432	0,997	34,937	0,996
L ₀	27,631	0,976	34,346	0,986	34,143	0,989	33,189	0,992
d-LCI	Inf	1,000	57,147	1,000	Inf	1,000	62,744	61,000
US12 400×266								
BIC	35,698	0,993	35,639	0,993	035,645	0,993	35,647	0,993
DPID	38,626	0,997	37,345	0,996	36,898	0,995	36,471	0,995
L ₀	29,883	0,972	32,902	0,978	33,091	0,982	33,776	0,987
d-LCI	Inf	1,000	55,801	1,000	Inf	1,000	62,744	1,000
US13 310×400								
BIC	38,220	0,996	38,166	0,996	38,173	0,996	38,177	0,996
DPID	41,001	0,998	39,707	0,997	39,276	0,997	38,861	0,997
L ₀	31,593	0,982	35,761	0,989	35,898	0,991	36,263	0,993
d-LCI	Inf	1,000	57,905	1,000	Inf	1,000	65,535	1,000

Table 6: Performance results on 13US dataset for high downscaling

	:20		:21		:27		:30		:33	
	PSNR	SSIM	PSNR	SSIM	PSNR	SSIM	PSNR	SSIM	PSNR	SSIM
US1 300×400										
BIC	38,583	0,996	38,585	0,996	38,586	0,996	38,585	0,996	38,584	0,996
d-LCI	66,485	1,000	Inf	1,000	Inf	1,000	70,845	1,000	Inf	1,000
US2 400×300										
BIC	33,302	0,987	33,302	0,987	33,302	0,987	33,303	0,987	33,303	0,987
d-LCI	66,347	1,000	Inf	1,000	Inf	66,092	1,000	1,000	Inf	1,000
US3 300×400										
BIC	43,786	0,999	43,787	0,999	43,786	0,999	43,788	0,999	43,784	0,999
d-LCI	69,721	1,000	Inf	1,000	Inf	1,000	74,415	1,000	Inf	1,000
US4 300×400										
BIC	40,633	0,996	40,634	0,996	40,636	0,996	49,636	0,996	49,635	0,996
d-LCI	68,054	1,000	Inf	1,000	Inf	1,000	71,936	1,000	Inf	1,000
US5 400×300										
BIC	30,311	0,979	30,311	0,979	30,311	0,979	30,311	0,979	30,311	0,979
d-LCI	59,853	1,000	Inf	1,000	Inf	1,000	63,768	1,000	Inf	1,000
US6 300×400										
BIC	30,311	0,979	29,663	0,978	29,664	0,978	29,663	0,978	29,663	0,978
d-LCI	59,135	1,000	Inf	1,000	Inf	1,000	62,833	1,000	Inf	1,000
US7 273×400										
BIC	40,524	0,995	40,521	0,995	40,524	0,995	40,536	0,995	40,520	0,995
d-LCI	67,318	1,000	Inf	1,000	Inf	1,000	72,151	1,000	Inf	1,000
US8 322×400										
BIC	31,808	0,989	31,807	0,989	31,807	0,989	31,807	0,995	31,806	0,989
d-LCI	63,539	1,000	Inf	1,000	Inf	1,000	67,653	1,000	Inf	1,000
US9 322×400										
BIC	28,354	0,984	28,355	0,984	28,354	0,984	28,355	0,984	28,355	0,984
d-LCI	58,651	1,000	Inf	1,000	Inf	1,000	62,536	1,000	Inf	1,000
US10 400×307										
BIC	35,174	0,992	35,172	0,992	35,174	0,992	35,175	0,992	35,175	0,992
d-LCI	63,924	1,000	Inf	1,000	Inf	1,000	67,994	1,000	Inf	1,000
US11 400×241										
BIC	34,535	0,995	34,535	0,995	34,534	0,995	34,534	0,995	34,535	0,995
d-LCI	63,445	1,000	Inf	1,000	Inf	1,000	67,442	1,000	Inf	1,000
US12 400×266										
BIC	35,647	0,993	35,646	0,993	35,645	0,993	35,646	0,993	35,648	0,993
d-LCI	63,760	1,000	Inf	1,000	Inf	1,000	67,127	1,000	Inf	1,000
US13 310×400										
BIC	38,175	0,996	38,175	0,996	38,174	0,996	38,175	0,996	38,175	0,996
d-LCI	66,347	1,000	Inf	1,000	Inf	1,000	70,960	1,000	Inf	1,000

obtained on 13US dataset for the scaling factors $s \in \{3, 6, 9, 18\}$ (Table 5) and for the larger factors $s \in \{20, 21, 27, 30, 33\}$ (Table 6).

According to the average results, the pointwise ones corroborate the global trend. In particular, Table 5 confirms that in downscaling d-LCI is the method allowing the largest PSNR and SSIM, and that the method requiring the least computation time is BIC, followed by d-LCI which is faster than DPID and L_0 . Also, note that the scaling factors chosen in Table 5 are all multiple of three but, according to Proposition 4.1 we can see the difference between the odd and even downscaling factors. Moreover, we can affirm that d-LCI works fine also for large downscaling factors as reported in Table 6 where the target images in 13US have been zoomed in up to 33 times, getting input images whose size goes up to 13200×10230 . We point out that in Table 6 the results for DPID and L_0 methods are missing because the publicly available MatLab codes don't work for so large scale factors. Moreover, if $s \in \{21, 27, 33\}$ then, in accordance with Proposition 4.1, PSNR and SSIM again reach the limit values Infinite and 1, respectively, by d-LCI while the same does not hold for BIC applied to the same input images.

6. Conclusions

In the context of interpolation methods for image resizing, we present the Lagrange–Chebyshev Interpolation (LCI) method. It is based on a non standard mathematical modeling that leads to the application of such an optimal Lagrange interpolation process to globally approximate the image at a continuous scale. One of the main advantages of LCI method is its high flexibility of working in both the scaling directions, either setting a scale factor or giving a particular final size. Comparisons with other resizing procedures have been reported on 5 different common datasets made of 726 images in total. The numerical experience in upscaling shows a performance comparable with the bicubic interpolation method, while in downscaling a much better performance is obtained with respect to all the considered comparison methods. Moreover, in downscaling cases with odd scale factors, we estimate the Mean Square Error (MSE) of our procedure in terms of the initial errors present in the data and we prove that it is null in absence of noise or artifacts in the input image. We wonder whether further improvements can be achieved employing wavelets technique or finer approximation polynomials. These will be the subjects of further investigations.

Code and supplementary materials

The code and the supplementary materials are openly available (to appear at a GitHub link).

References

- [1] <http://sipi.usc.edu/database/>.
- [2] <https://www.gcc.tu-darmstadt.de/home/proj/dpid/index.en.jsp>.

- [3] <http://www.shengfenghe.com/publications/>.
- [4] <https://www2.eecs.berkeley.edu/Research/Projects/CS/vision/bsds/>.
- [5] <https://www.cl.cam.ac.uk/~aco41/Files/Sig15UserStudyImages.html>.
- [6] National aeronautics and space administration. NASA image gallery, 2016.
- [7] C. Arcelli, N. Brancati, M. Frucci, G. Ramella, and G. Sanniti di Baja. A fully automatic one-scan adaptive zooming algorithm for color images. *Signal Processing*, 91(1):61–71, 2011.
- [8] P. M. Atkinson. Downscaling in remote sensing. *International Journal of Applied Earth Observation and Geoinformation*, 22:106–114, 2013.
- [9] L. Bos, M. Caliari, S. De Marchi, M. Vianello, and Y. Xu. Bivariate Lagrange interpolation at the Padua points: the generating curve approach. *J. Approx. Theory*, 143:15–25, 2006.
- [10] V. Bruni, G. Ramella, and D. Vitulano. Automatic perceptual color quantization of dermoscopic images. *VISAPP 2015, J. Braz et al. Eds., Scitepress Science and Technology Publications*, 1:323–330, 2015.
- [11] M. Caliari, S. De Marchi, and M. Vianello. Bivariate Lagrange interpolation at the Padua points: computational aspects. *J. Comput. Appl. Math.*, 221:284–292, 2008.
- [12] J. Chaki and N. Dey. Introduction to image color feature. In *Springer-Briefs in Applied Sciences and Technology*, Singapor, 2021.
- [13] G. Chen, Zhao H., C. K. Pang, T. Li, and C. Pang. Image scaling: How hard can it be? *IEEE Access*, 7, 2019.
- [14] S. De Marchi, W. Erb, and F. Marchetti. Spectral filtering for the reduction of the Gibbs phenomenon for polynomial approximation methods on Lissajous curves with applications in MPI. *Dolom. Res. Notes Approx.*, 10:128–137, 2017.
- [15] B. Fischer and J. Prestin. Wavelets based on orthogonal polynomials. *Math. Comp.*, 66:1593–1618, 1997.
- [16] B. Fischer and W. Themistoclakis. Orthogonal polynomial wavelets. *Numer. Alg.*, 30:37–58, 2002.
- [17] J.-B. Huang, A. Singh, and N. Ahuja. Single image super-resolution from transforme self-exemplars. *Proc. CVPR*:5197–5206, 2015.
- [18] C. Kaethner, W. Erb, M. Ahlborg, P. Szwargulski, T. Knopp, and T. M. Buzug. *IEEE Transactions on Medical Imaging*, 35(11):2476–2485, 2016.
- [19] R. Keys. Cubic Convolution Interpolation for Digital Image Processing. *IEEE Transactions on Acoustics, Speech, and Signal Processing*, 29(6):1153–1160, 1981.
- [20] T. Kilgore and J. Prestin. Polynomial wavelets on the interval. *Constr. Approx.*, 12:95–110, 1996.

- [21] T. Knopp and T. M. Buzug. *Magnetic Particle Imaging*. Springer-Verlag Berlin Heidelberg, Berlin, 2012.
- [22] H. Liu, X. Xie, W.Y. Ma, and H.J. Zhang. Automatic Browsing of Large Pictures on Mobile Devices. In *11th ACM International Conference on Multimedia, CA, USA, 2003*. Berkeley.
- [23] J. Liu, S. He, and R. W. H. Lau. L_0 -Regularized Image Downscaling. *IEEE Trans. Image process.*, 27(3):1076–1085, 2018.
- [24] T. Liu, Z. Yuan, J. Sun, J. Wang, N. Zheng, X. Tang, and H.-Y. Shum. Learning to detect a salient object. *IEEE Trans. on Patt. Anal. Mach. Intell.*, 33(2):353–367, 2011.
- [25] A. Lookingbill, J. Rogers, D. Lieb, J. Curry, and S. Thrun. Reverse Optical Flow for Self-Supervised Adaptive Autonomous Robot Navigation. *International Journal of Computer Vision*, 74(3):287–302, 2007.
- [26] D. Martin, C. Fowlkes, D. Tal, and J. Malik. A database of human segmented natural images and its application to evaluating segmentation algorithms and measuring ecological statistics. In *Proc. 8th Int. Conf. Computer Vision*, volume 2, pages 416–423, 2001.
- [27] G. Mastroianni and G. V. Milovanovic. *Interpolation Processes Basic Theory and Applications*. Springer Monographs in Mathematics. Springer Verlag, Berlin, 2009.
- [28] E. H.W. Meijering, W. J. Niessen, and M. A. Viergever. Quantitative evaluation of convolution-based methods for medical image interpolation. *Medical Image Analysis*, 5:111–126, 2001.
- [29] H. Mittal, A.C. Pandey, M. Saraswat, and et al. A comprehensive survey of image segmentation: clustering methods, performance parameters, and benchmark datasets. *Multimed Tools Appl*, 2021.
- [30] C.H. Neetha, C. John Moses, and D. Selvathi. Image interpolation using non-adaptive scaling algorithms for multimedia applications. a survey. In *Advances in Automation, Signal Processing, Instrumentation, and Control, Komanapalli V.L.N., Sivakumaran N., Hampannavar S. (eds)*, volume 700, pages 1509–1516, 2021.
- [31] D. Occorsio and M. G. Russo. Numerical methods for Fredholm integral equations on the square. *Appl. Math. and Comput.*, 218(5):2318–2333, 2011.
- [32] D. Occorsio and W. Themistoclakis. Uniform Weighted Approximation by Multivariate Filtered Polynomials. *Lecture Notes in Computer Science (including subseries Lecture Notes in Artificial Intelligence and Lecture Notes in Bioinformatics)*, 11973 LNCS:86–100, 2020.
- [33] D. Occorsio and W. Themistoclakis. Uniform weighted approximation on the square by polynomial interpolation at Chebyshev nodes. *Appl. Math. and Comput.*, 385(125457), 2020.

- [34] D. Occorsio and W. Themistoclakis. On the filtered polynomial interpolation at Chebyshev nodes. *Appl. Numer. Math.*, 166:272–287, 2021.
- [35] D. Occorsio and W. Themistoclakis. Some remarks on filtered polynomial interpolation at Chebyshev nodes. *Dolom. Research. Notes on Approx.*, 14:68–84, 2021.
- [36] A. C. Oztireli and M. Gross. Perceptually based downscaling of images. *ACM Trans. Graph.*, 34(4):1–10, 2015.
- [37] G. Plonka, D. Potts, G. Steidl, and M. Tasche. *Numerical Fourier Analysis. Applied and Numerical Harmonic Analysis*. Birkhäuser Springer Nature Switzerland AG, Berlin.
- [38] G. Ramella. Evaluation of quality measures for color quantization. *Multimedia Tools and Applications*, 2021.
- [39] G. Ramella and G. Sanniti di Baja. Color histogram-based image segmentation. *Lecture Notes in Computer Science*, 6854:76–83, 2011.
- [40] G. Ramella and G. Sanniti di Baja. Image segmentation based on representative colors and region merging. In *Pattern Recognition, J. A. Carrasco-Ochoa et al Eds.*, volume 7914, pages 175–184, 2013.
- [41] G. Ramella and G. Sanniti di Baja. A new technique for color quantization based on histogram analysis and clustering. *Int. J. Patt. Recog. Artif. Intell.*, 27(3):1–17, 2013.
- [42] G. Ramella and G. Sanniti di Baja. From color quantization to image segmentation. In *Signal Imag. Techn. Internet-Based Syst. - SITIS 2016, K. Yetongnon et al. Eds.*, pages 798–804, 2016.
- [43] G. Ramella and G. Sanniti di Baja. A new method for color quantization. In *Signal Imag. Techn. Internet-Based Syst. - SITIS 2016, K. Yetongnon et al. Eds.*, pages 1–6, 2016.
- [44] B. Thomee, D.A. Shamma, G. Friedland, B. Elizalde, K. Ni D. Poland, D. Borth, and L.-J. Li. Yfcc100m: The new data in multimedia research. *Communications of the ACM*, 59(2):64–73, 2016.
- [45] L. N. Trefethen. *Approximation theory and approximation practices*. Society for Industrial and Applied Mathematics (SIAM), Philadelphia, PA, 2013.
- [46] T. Vlašić, I. Ralašić, A. Tafro, and D. Seršić. Spline-like Chebyshev polynomial model for compressive imaging. *J. Vis. Commun. Image*, 66(102731):370–378, 2020.
- [47] N. Weber, M. Waechter, S. C. Amend, S. Guthe, and M. Goesele. Rapid detail-preserving image downscaling. *ACM Trans. Graph.*, 35(6):1–6, 2016.
- [48] Y. Xu. Lagrange interpolation on Chebyshev points of two variables. *J. Approx. Theory*, 87(2):220–238, 1996.

- [49] Y. Xu. Minimal cubature rules and polynomial interpolation in two variables ii. *J. Approx. Theory*, 214:49–68, 2017.
- [50] T. Yao, Y. Luo, Y. Chen, D. Yang, and L. Zhao. Single-image Super-Resolution: A survey. In *CSPS 2018*, Liang Q., Liu X., Na Z., Wang W., Mu J., Zhang B. (eds), volume 516, pages 119–125, 2020.
- [51] M. Zhang, L. Zhang, Y. Sun, L. Feng, and W. Ma. Auto cropping for digital photographs. In *Signal Imag. Techn. Internet-Based Syst. - SITIS 2016*, K. Yetongnon et al. Eds., 2005.